Operational Monitoring and Damage Assessment of Riverine Flood-2014 in the Lower Chenab Plain, Punjab, Pakistan, Using Remote Sensing and GIS Techniques

Asif Sajjad [1], Jianzhong Lu [1,*] , Xiaoling Chen [1], Chikondi Chisenga [1,2] , Nayyer Saleem [1] and Hammad Hassan [1]

[1] State Key Laboratory of Information Engineering in Surveying, Mapping and Remote Sensing, Wuhan University, Wuhan 430079, China; asifsajjad@whu.edu.cn (A.S.); xiaoling_chen@whu.edu.cn (X.C.); cchisenga@must.ac.mw (C.C.); saleemnayyer@whu.edu.cn (N.S.); hhrizvi@whu.edu.cn (H.H.)

[2] Department of Earth Sciences, Ndata School of Climate and Earth Sciences, Malawi University of Science and Technology, Limbe P.O. Box 5196, Malawi

* Correspondence: lujzhong@whu.edu.cn; Tel.: +86-27-6877-8755; Fax: +86-27-6877-8229

check for updates

Abstract: In flood-prone areas, the delineation of the spatial pattern of historical flood extents, damage assessment, and flood durations allow planners to anticipate potential threats from floods and to formulate strategies to mitigate or abate these events. The Chenab plain in the Punjab region of Pakistan is particularly prone to flooding but is understudied. It experienced its worst riverine flood in recorded history in September 2014. The present study applies Remote Sensing (RS) and Geographical Information System (GIS) techniques to estimate the riverine flood extent and duration and assess the resulting damage using Landsat-8 data. The Landsat-8 images were acquired for the pre-flooding, co-flooding, and post-flooding periods for the comprehensive analysis and delineation of flood extent, damage assessment, and duration. We used supervised classification to determine land use/cover changes, and the satellite-derived modified normalized difference water index (MNDWI) to detect flooded areas and duration. The analysis permitted us to calculate flood inundation, damages to built-up areas, and agriculture, as well as the flood duration and recession. The results also reveal that the floodwaters remained in the study area for almost two months, which further affected cultivation and increased the financial cost. Our study provides an empirical basis for flood response assessment and rehabilitation efforts in future events. Thus, the integrated RS and GIS techniques with supporting datasets make substantial contributions to flood monitoring and damage assessment in Pakistan.

Keywords: floods; Landsat-8; remote sensing; GIS; disaster mapping; damage assessment; Lower Chenab Plain

1. Introduction

Flood disasters are among the most frequent and destructive of all-natural disasters, posing a potential threat to life and property. Every year, human lives, agricultural activities, and infrastructures are seriously affected by shattering flood disasters around the globe [1–3]. In the past three decades, flood disasters affected nearly 2.8 billion people and resulted in over 200,000 causalities with substantial damages to property and economy [4]. Floods account for ~47% of all weather-related disasters that occur across the world [5]. Climate change and rapid population increases in floodplains enforce and boost the frequency and magnitude of riverine flood damages [6,7].

As flood disasters increase in magnitude, the Asian region continues to face a large number of flood hazards and associated losses in lives and all kinds of infrastructure and economic progress [4,7]. In recent years, the south Asia region has been experiencing intense flooding with increased frequency, especially in Pakistan [8–10].

In Pakistan, flood events are recognized as a major natural hazard that historically originates from the Indus and Chenab rivers [11–13]. Since the creation of Pakistan, 1955, 1959, 1973, 1976, 1988, 1992, 1995, 1996, 1997, 2006, 2010, and 2014 are recorded as the years for destructive floods that resulted in adverse impacts on human lives, property, and the country's economy [9,14,15]. Floods in Pakistan mostly occur in the monsoon months of July and September, due to heavy rains and the melting of snow upstream in the Himalaya region. This results in riverine floods that produce tremendous detrimental impacts on human lives, agriculture, and infrastructure [16–18]. For instance, the 2010 riverine flood caused a large inundation that covered an area of 70,238 km^2, with 884,715 affected houses [8,12,18]. Likewise, the 2011 flood affected 5.88 million people and damaged standing crops and infrastructure covering an area of 16,440 km^2 and 1882 km^2, respectively [19]. In 2014, heavy rains coupled with the melting of glaciers in the upstream part of Chenab caused flash flooding in mountainous areas and riverine floods in the upper and lower Chenab plain [20–22]. It was considered one of the worst riverine flood catastrophes in terms of damages to standing crops, housing, and infrastructure along the floodplain areas of the Chenab river [13,16,22,23]. This indicates that flooding is a serious problem in Pakistan that requires significant efforts to reduce its effects, mainly through effective post-disaster monitoring and management, especially in the Chenab plain [22–24]. As such, we provide a scientific basis that provides a rapid flood 2014 mapping and monitoring using Landsat-8 data, with a focus on the lower Chenab plain. We first provide the limitation of previous studies on the riverine flood of 2014 that focused less on post-flood mapping, monitoring, and damage assessment. These previous studies mainly focused on the upper Chenab plain [13,16,21,22] without focusing on the lower Chenab plain. This is despite the fact that the lower Chenab plain is a fertile flood-prone plain and considered an economically underdeveloped region in the Punjab province of Pakistan. Despite being an understudied area, negligence adds to the problems with a lack of localized flood management strategies. Therefore, accurate post-flood mapping, monitoring, and evaluating damages are the utmost requirements for rapid flood risk assessment in lower Chenab plain. Secondly, to a basis for rapid flood risk mapping, we make use of multispectral remote sensing open data in conjunction with Geographical Information System (GIS) techniques for monitoring and evaluating damage assessment in the severely flood-affected areas of the lower Chenab plain, Punjab, Pakistan.

The use of remote sensing and GIS techniques is chosen as it contributes to an exploration of flood causes and additionally provides accurate mapping of flood extents that enables detailed investigations of flood instances [18,19,25]. Moreover, these techniques can be applied in damage assessment to standing crops and infrastructure. Effective flood modeling and mapping are important for flood assessment, loss estimation, and sustainable land use planning along flood plains to mitigate flood risk effectively [25,26]. Multi-temporal remote sensing images provide a wide source of low-cost information with a reliable accuracy that can be beneficially utilized for flood mapping [27,28]. Furthermore, multispectral remote sensing-derived indexes and GIS-based classifications can be exploited to detect flooded areas [18,29,30]. a wide range of open-source remote sensing data has permitted valuable and accurate historical data, which is essential for a comprehensive study on flood disaster mapping and damage assessment [31]. For example, moderate resolution Landsat data have provided free, up-to-date satellite images across the globe since 1972, which can be used for flood disaster monitoring and damage assessment [32,33]. High-resolution Google Earth (GE) images provide historical and recent data that can also be used for flood monitoring and temporal flood mapping [34]. GE images can also be used as input datasets to digitize land uses, particularly useful in small areas [5], and for the validation of supervised classified images [35]. Thus, the current study uses remote sensing and GIS techniques to detect flood inundation and duration, and evaluate flood damages on different land uses, such as agricultural land and built-up areas. We used the identified

relationship between land uses and flood instances to estimate the overall damage, flood extent, and propose emergency flood management for future floods on the lower Chenab plain.

2. Materials and Methods

2.1. Study Area

The study area is the lower Chenab plain, which is located in the downstream part of river Chenab, central Pakistan. It is located between 70°41′13.2″E and 29°6′0″N, and 71°37′58.8″E and 30°31′33.6″N, within the three main districts of Punjab province, namely the Multan, Muzaffar Garh, and Bahawalpur districts (Figure 1). It is one of the fertile plains of Punjab province, where floods occur almost every year. The Chenab river originates from the Indian state of Himachal Pradesh. Then, it flows through Indian-occupied Kashmir and enters at Marala Headwork into the province of Punjab, Pakistan. The southern part of the study area includes the Panjnad Barrage where the Sutlej River joins the Chenab, as shown in Figure 1. The total length of the River Chenab is about 974 km, of which 729 km fall within Pakistan. Of the 729 km, we selected approximately 215 km as our study area. We then divided the 215 km into three equal sections, each approximately 71 km long (Figure 1), to enable the visualization and detailed investigation of the results. We also created a 6-km-wide buffer around the Chenab River that covers a distance of about 215 km from north to south as the final extent of our study area. The mean annual Chenab discharge is 1.52 million m^3 [36,37]. The highest temperature documented in the study area is 50 °C in the month of June with the lowest recorded temperature of 2 °C in the month of January [20]. The average yearly rainfall is 157 mm, with July receiving a maximum of 45 mm and October receiving a minimum of only 2mm [20]. The main source of livelihood in the study area is agriculture with main crops being sugarcane, cotton, maize, rice, and fodder.
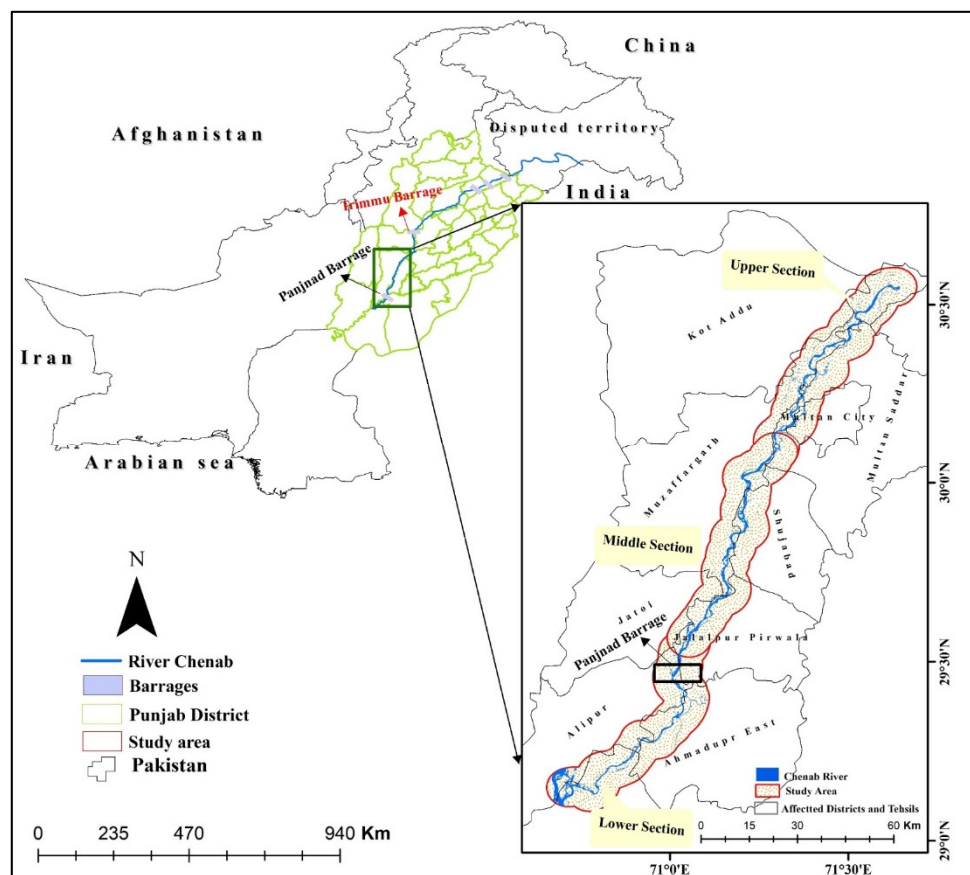
Figure 1. Location of the lower Chenab plain in Pakistan, and the zoomed area represents the river Chenab system, and also shown is the 6-km buffer zone and the extent of our study area.

2.2. Materials

The main data source of this study is Landsat 8 imagery (Table 1), acquired from the United States Geological Survey (USGS). Landsat images have a temporal resolution of ~16 days that has provided free up-to-date images across the globe since 1972 [22,33,38,39]. However, the study area provides a unique opportunity with a high temporal resolution of ~8 days since the area lies within two adjacent Landsat paths of 150 and 151 (Figure 2; Table 1), which enables us to make an in-depth analysis of the flood duration and inundation. In total, we used 9 temporal images acquired between 7 August and 27 November 2014 (Table 1). We used 8 temporal images for flood monitoring. Furthermore, we used 3 temporal images for flood damage assessment using land use/cover classification during flood instances in lower Chenab plain (Table 1).

We also used GPS and the Google Earth (GE) platform to collect spatial training datasets, which were used to support land use/cover classification. The GPS data were collected after the flood waters had ceased, as it was challenging to do field survey during flooding time, due to flood inundation. These points were also used to validate classification and inundation results. Due to its high resolution, the GE platform provides a better visualization of the real-world scenario of land use/cover change in the study area [34]. Furthermore, GE images of three flood instances (and with similar acquisition dates as the Landsat-8 images) were taken for cross-comparison with the Landsat-based land use/cover classification. The Pre-flood image was acquired on 4 August, 2014, the Co-flood image was taken on 13 September, 2014, and the closest available Post-flood image was acquired on 11 November, 2014. To further understand post-flood situation in the study area, a comprehensive field survey was conducted to identify damages and affected areas and observe the Post-flood effects and rehabilitation process.

Table 1. Specifications of used Landsat-8 data.

Path	Row	Date of Acquisition	Flood Instances	Use	Resolution (m)
151	39 and 40	7 August 2014	Pre-flood	Land-use classification	30
150	39 and 40	17 September 2014	Co-flood	Land-use classification and Flood monitoring	30
151	39 and 40	24 September 2014	Co-flood	Flood monitoring	30
150	39 and 40	3 October 2014	Post-flood	Flood monitoring	30
151	39 and 40	10 October 2014	Post-flood	Flood monitoring	30
150	39 and 40	19 October 2014	Post-flood	Flood monitoring	30
151	39 and 40	26 October 2014	Post-flood	Flood monitoring	30
151	39 and 40	11 November 2014	Post-flood	Flood monitoring	30
151	39 and 40	27 November 2014	Post-flood	Land-use classification and Flood monitoring	30
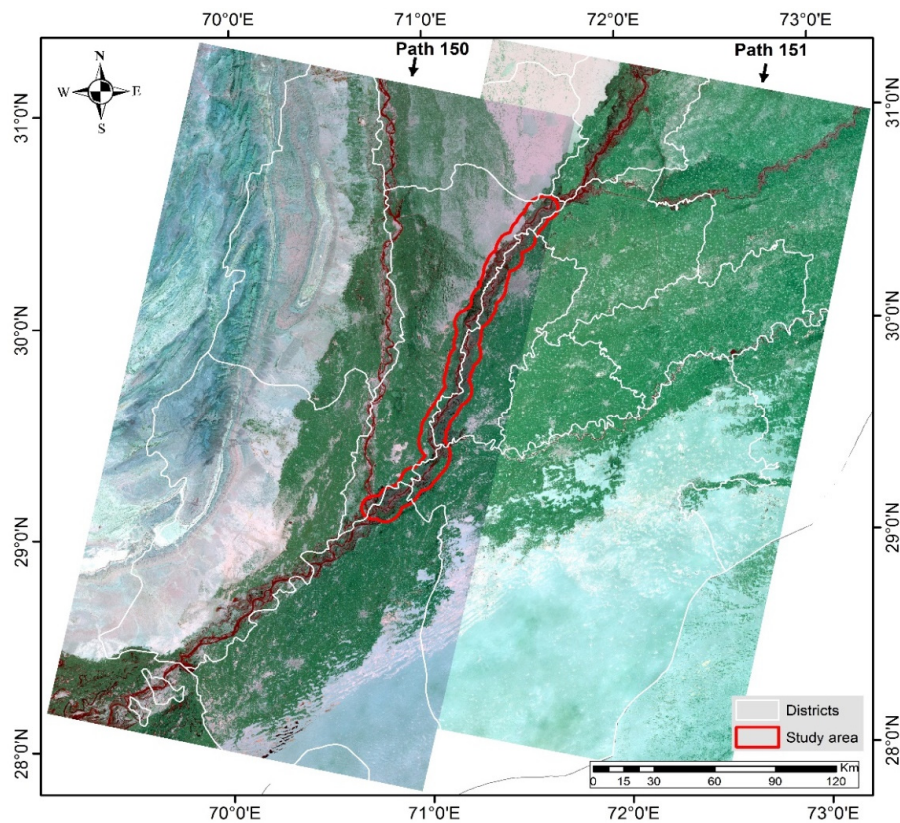
Figure 2. Landsat satellite images: Path 150 and 151 show the study area and districts.

2.3. Methods

The overview of the used methodology is presented in Figure 3. Firstly, we applied radiometric correction, layer stacking and mosaicking and resampling to the Landsat-8 images before use. Then, we converted the digital number values on the Landsat images to reflectance using ENVI's Radiometric Calibration Tool [18]. Finally, we used Arc GISs' spatial analysis tools for Layer stacking and mosaicking, and resampling. The pre-processed Landsat-8 pre-flood, co-flood, and post-flood images were subjected to supervised classification for land use/cover mapping in ArcGIS 10.5, as shown in Figure 3. Landsat data are most common and is often used for different land use/cover mapping and water extraction mapping [13,40]. The Supervised classification method is used to extract information from Landsat data [29,41]. In addition, a maximum likelihood (ML) approach was applied for land

use/land cover classification of flood instances. The ML approach is widely used and is easy to apply for land use/cover classification. The ML approach has also been applied to land use/cover mapping of pre-flooding, co-flooding, and post-flooding [11,18,22,39–42]. We identified water, agriculture land, and vegetation, built up, sand, barren land, and deposited material as the six land-use classes in the study region. To facilitate the ML approach for classification, a total of 360 spatial training samples were collected from a GPS field survey and comparatively high-resolution GE images, and were further assigned to the pixel values of the most probable land use/cover class. All spatial training datasets were compiled and prepared in Microsoft Excel and were imported into the Arc GIS 10.5 environment. The classified images were converted into a shapefile format and used as input for the GIS-based spatial overlay analysis. This allows us to spatially compare and intersect all classified land uses to provide a clear picture of flood inundated and damaged land uses in lower Chenab.
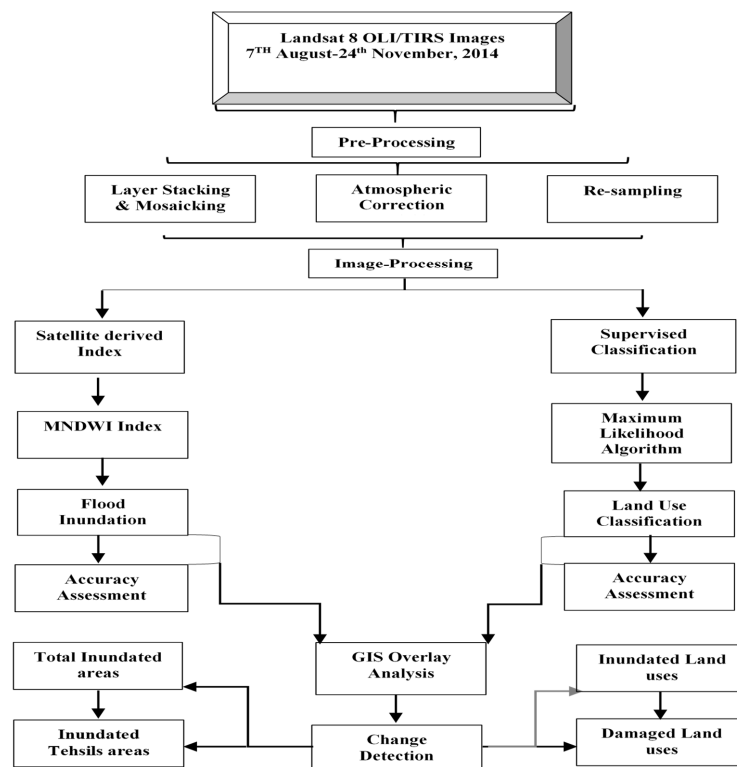

Figure 3. Methodological framework for the flood inundation mapping and damage assessment using multi-temporal Landsat-8 images.

For damage assessment, we defined a damaged area as an area that experienced a change from 'agricultural' and 'built up' in pre-flood to 'deposited material' in post-flood. a pre-flood image was used as a reference and a change detection technique was used to evaluate damages to agriculture and built-up areas in the study area.

2.3.1. MNDWI Index

The Modified Normalized Difference in Water Index (MNDWI) was used to delineate the spatial pattern of flood-2014 inundation along the lower Chenab plain. The MNDWI index is widely used for the rapid delineation of floodwater required for flood monitoring and assessment, and has been compared to other indices, i.e., the NDWI and Water Ratio Index (WRI) [43,44]. The Normalized Difference Water Index (NDWI) presented by McFeeters [45], is very efficient at delineating water information but has difficulties in case a built-up area exists in water environment. Therefore, Xu [46] presented an effective MNDWI index, which is much better at distinguishing between water and

built-up areas. The MNDWI is calculated using green (Band 3) and shortwave infrared (Band 6) wavelengths to delineate water, as given by Equation (1):

$$MNDWI = \frac{(\text{Band3}) - (Band\ 6)}{(Band3) + (Band6)} \tag{1}$$

where GREEN (Band 3) = Green wavelength (0.53–0.59mm) and SWIR (Band 6) = Short-wave infrared Wavelength (1.57–1.65 mm)

This index is utilized for the removal of built-up area noise, and it uses Band 3 wavelength to maximize water reflectance. The resulting value ranges from −1 to +1. The low water reflectance and high reflectance of built-up in Band 6 result in positive values of water and negative values of built up in the MNDWI image. The limitation of the MNDWI index is that it does not efficiently distinguish between hill shadow and water body [47,48]. From literature, the MNDWI index has been used for the extraction of water on a flat plain with scattered built-up areas using Landsat 8 OLI and SAR data, achieving high accuracy and better performance. Thus, it was also strongly recommended, in comparison with other indexes, to be applied on Landsat images [49–52].

2.3.2. Classification and Inundation Validation

The classified images and index-derived inundation were validated using GPS and Google earth (GE) points. For this, the random sample points' tool within the Arc GIS spatial analyst was used to extract random points on the classified land uses of inundated and non-inundated images. These points were then converted into a kml format and overlaid on GE. The values of these points were evaluated using visual interpretation and expert knowledge. The accuracy of classified images was assessed using 557 Arc GIS random points and 150 GPS points. We have used 30 Arc GIS random points of class, namely: water, agriculture, built-up, barren, sand, and deposited material, to each flood instance image. In addition to this, we have further used 25 GPS points of above-mentioned classes to only post-flood instance for the validation process. The accuracy of inundation maps was assessed using 400 ArcGIS random points and 200 GPS points. Furthermore, for each inundation map, we have used 50 ArcGIS random points and 25 GPS points for the validation of water and non-water classes. Lastly, the results from the comparison of random samples and GPS with GE images were used to create the confusion matrix. The confusion matrix was used to evaluate the accuracy of the ML land use/cover classification and MNDWI inundation. We also used the Kappa Coefficient (KC) as an indicator to validate the qualitative agreement, either positive or negative, between classified samples and ground-truth points. It is normally calculated from a statistical assessment to evaluate the proportional improvement by the classifier over ground-truth samples to land-use classes.

3. Results

3.1. Accuracy Assessment

The overall inundation accuracy obtained from all images is above 90%, as shown in Table 2. The highest overall accuracy of 92% is obtained from the peak-flood image (17 September) and the post-flood image (27 November), while the least overall accuracy of 88% is acquired from the post-flood (11 November) image. Similarly, the obtained average user and producer accuracy of both classes is nearly 90%. The highest user accuracy of the water class is attained from the peak-flood image (17 September), which is 96%, and the least is 85%, which is obtained from the post-flood (11 November) image. On the other hand, the highest user accuracy of the non-water class is achieved from the post-flood (27 November) image, which is 93%, and the least is 86%, which is from the peak-flood (17 September) image. Furthermore, the highest attained producer accuracy of the water class is 94% from the post-flood (26 October) image, and the least is 87% from the peak-flood (17 September) image. The highest obtained non-water class producer accuracy is 96% from the peak-flood (17 Sepember) image and the least is 86%, which is obtained from the post-flood (11 November) image. The highest

KC accuracy of 85% is achieved from the post-flood (27 November) image and the least KC accuracy is obtained from the post-flood (11 November) image. The average KC accuracy of all the images is above 80% (Table 2).

The highest overall supervised classification accuracy obtained is 92% from the post-flood image. Whereas, the lowest accuracy of 85% was obtained from the co-flood image, as shown in Table 3. The KC accuracy shows that the highest accuracy of 90% is obtained from the post-flood (27 November) image and that the lowest of 81% is obtained from the co-flood (17 September) image. Similarly, the user and producer accuracies were also calculated, which are listed in Table 3. The highest user accuracy was attained by water, barren land, and sand classes of 92%, 96%, and 99%, respectively. Likewise, the highest producer accuracy was obtained by the water, built-up area, and deposited material classes at 99%, 98%, and 95%, respectively. The overall land-use classification accuracy suggests that classified images are reliable for further analysis.

Table 2. Accuracy assessment of the modified normalized difference water index (MNDWI)-derived flood 2014-inundation.

Classes	17 September 2014				24 September 2014				3 October 2014				10 October 2014			
	PA	UA	OA	KC	PA	UA	OA	KC	PA	UA	OA	KC	PA	UA	OA	KC
Water	0.87	0.96	0.92	0.84	0.91	0.93	0.91	0.83	0.88	0.92	0.90	0.81	0.91	0.90	0.90	0.81
Non-Water	0.96	0.86			0.93	0.91			0.91	0.88			0.90	0.92		
Classes	19 October 2014				26 October 2014				11 November 2014				27 November 2014			
	PA	UA	OA	KC	PA	UA	OA	KC	PA	UA	OA	KC	PA	UA	OA	KC
Water	0.91	0.91	0.90	0.80	0.94	0.86	0.90	0.81	0.91	0.85	0.88	0.76	0.93	0.91	0.92	0.85
Non-water	0.90	0.92			0.87	0.90			0.86	0.92			0.92	0.93		

PA = Producer Accuracy; UA = User Accuracy; OA = Overall Accuracy; KC = Kappa Coefficient

Table 3. Accuracy assessment of supervised classified land uses.

Classes	Pre-Flood Classified Image (7 August 2014)				Co-Flood Classified Image (17 September 2014)				Post-Flood Classified Image (17 September 2014)			
	PA	UA	OA	KC	PA	UA	OA	KC	PA	UA	OA	KC
water	0.95	0.92			0.92	0.92			0.99	0.88		
built up	0.95	0.80			0.83	0.76	0.85	0.81	0.98	0.84		
vegetation	0.70	0.88	0.86	0.83	0.87	0.80			0.92	0.92	0.92	0.90
barren	0.85	0.92			0.78	0.88			0.88	0.96		
sand	0.80	0.80			0.85	0.88			0.83	0.99		
Deposited material	0.95	0.86			-	-	-	-	0.92	0.92		

PA = Producer Accuracy; UA = User Accuracy; OA = Overall Accuracy; KC= Kappa Co-efficient.

3.2. Flood Mapping and Monitoring

The temporal flood 2014 extent maps were prepared and used to determine the most inundated areas in the study area, as a tool for flood monitoring. Figure 4a,b shows the flood inundation with a flood peak on 17 September, which remained stable until the 24 September, and then the inundation gradually decreased till post-flood 27 November. Figure 4a and Table 4 show that northwestern Muzaffargarh and northeastern Multan Saddar part was the most inundated and affected region along with the southeastern ShuJabad and Jalalpur Pirwala. The flooded area receded in three phases: In the first phase from 24 September to 10 October, the southern part gradually receded from west to east. The central part began to recede from 10–26 October 2014 in the second phase, and in the third phase, almost all the flood water receded until 27 November 2014. Hence, the flood duration result shows that Muzaffargarh and Multan Saddar remained inundated for almost two months and reported the most affected areas by flood-2014 in lower Chenab plain.
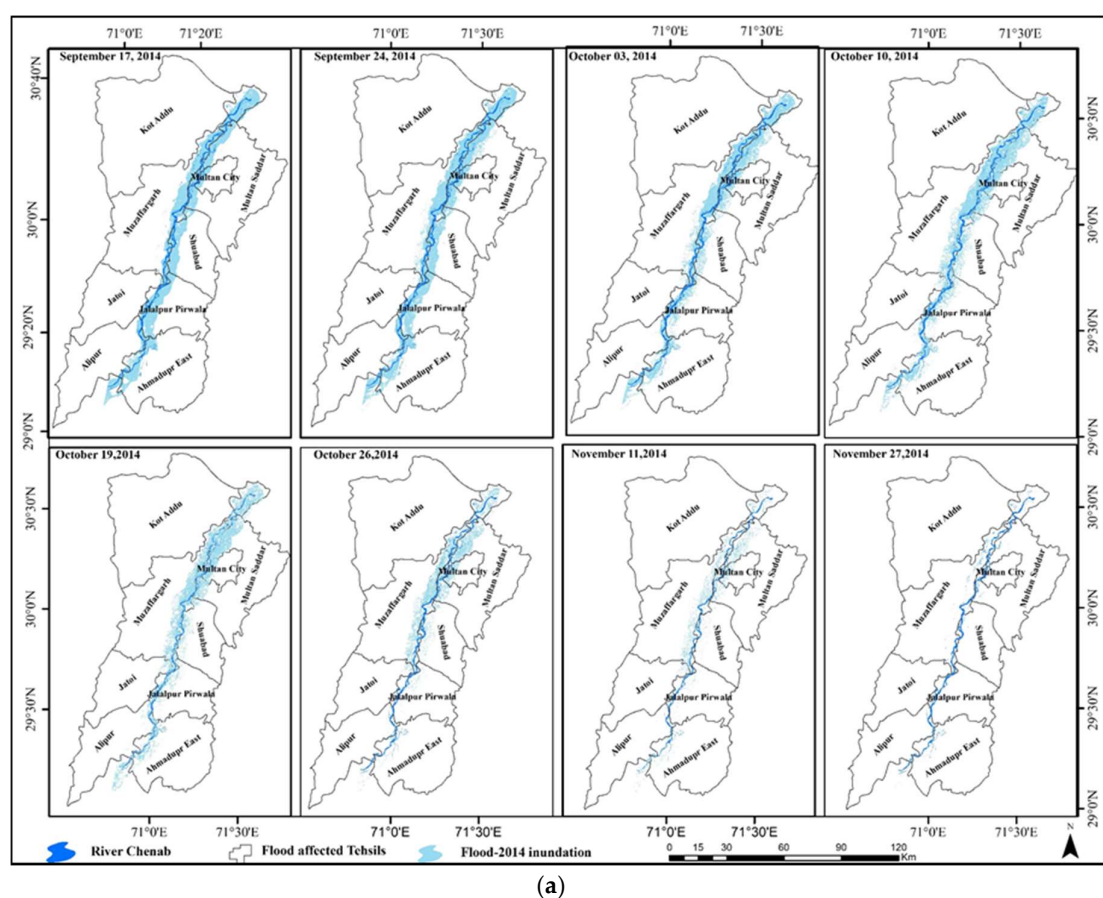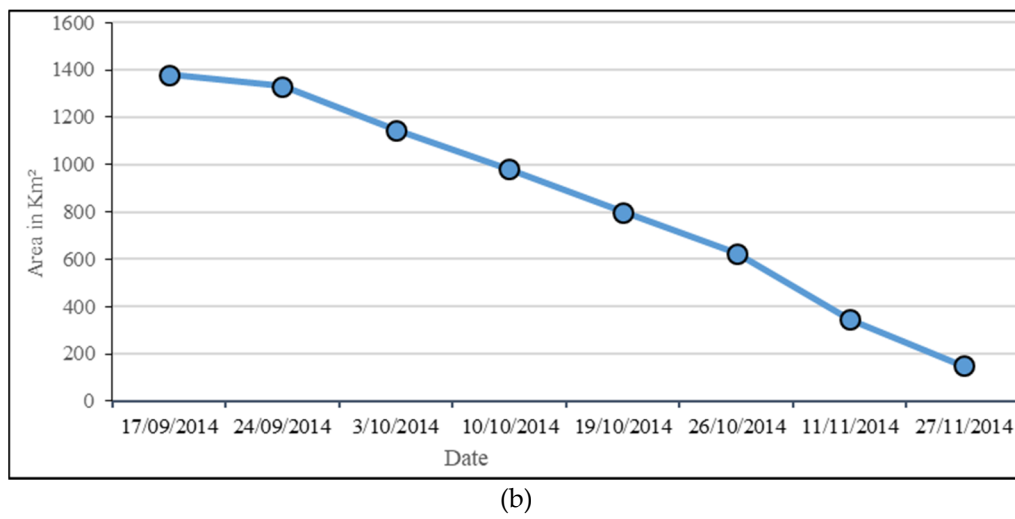

(**a**)

Figure 4. *Cont.*

(b)

Figure 4. (**a**) Comprehensive flood inundation and recession in the lower Chenab plain. (**b**) Flood recession in the lower Chenab plain from 17 September (peak-flood) to 27 November 2014 (post-flood).

Table 4. Inundated areas of the lower Chenab plain in Km^2.

Districts	Tehsils	17 September 2014	24 September 2014	3 October 2014	10 October 2014	19 October 2014	26 October 2014	11 November 2014	27 November 2014
Muzaffargarh	**Alipur**	58.87	57.02	50.86	34.31	26.24	15.66	12.34	11.14
	Muzaffargarh	530.53	507.99	485.48	409.12	363.56	308.75	166.25	68.93
	Kot Addu	2.41	2.77	2.45	2.82	2.13	1.55	0.71	0.42
	Jatoi	11.39	15.37	13.29	19.48	15.23	11.25	8.21	1.38
Multan	**Jalalpur Pirwala**	212.51	191.89	141.34	97.86	56.34	40.16	21.45	16.01
	ShuJabad	169.51	159.95	96.19	88.48	64.73	40.36	25.13	10.39
	Multan Saddar	209.21	223.26	212.56	205.03	188.45	147.9	74.32	22.80
	Multan City	37.43	42.58	41.95	39.72	39.67	35.78	17.65	3.7
Bahawalpur	**Ahmadupr East**	148.57	129.13	103.80	83.6	44.05	24.94	19.34	15.79
Total Area		**1380.43**	**1330.96**	**1147.92**	**980.54**	**800.4**	**626.35**	**345.4**	**146.56**

The peak-flood (17 September) extent is compared in Figure 5a,b. In Figure 5a, the MNDWI index shows the accumulated flood extent that covers an area of 1380km^2. Whereas, in Figure 5b, the classified image shows that about 1330.03 km^2 of the area was inundated, which represents a 2% deviation from the MNDWI results. The result shows that both the MNDWI index and supervised classification produce almost similar inundation areas in lower Chenab plain. Furthermore, these inundation results, when incorporated with the GE images acquired at the same time as the Landsat-8 images, also showed the severe spatial pattern of inundation, and they also validate our estimated flood inundation extent, confirming that flood waters remained for almost two months and receded very slowly (Section 3.3).
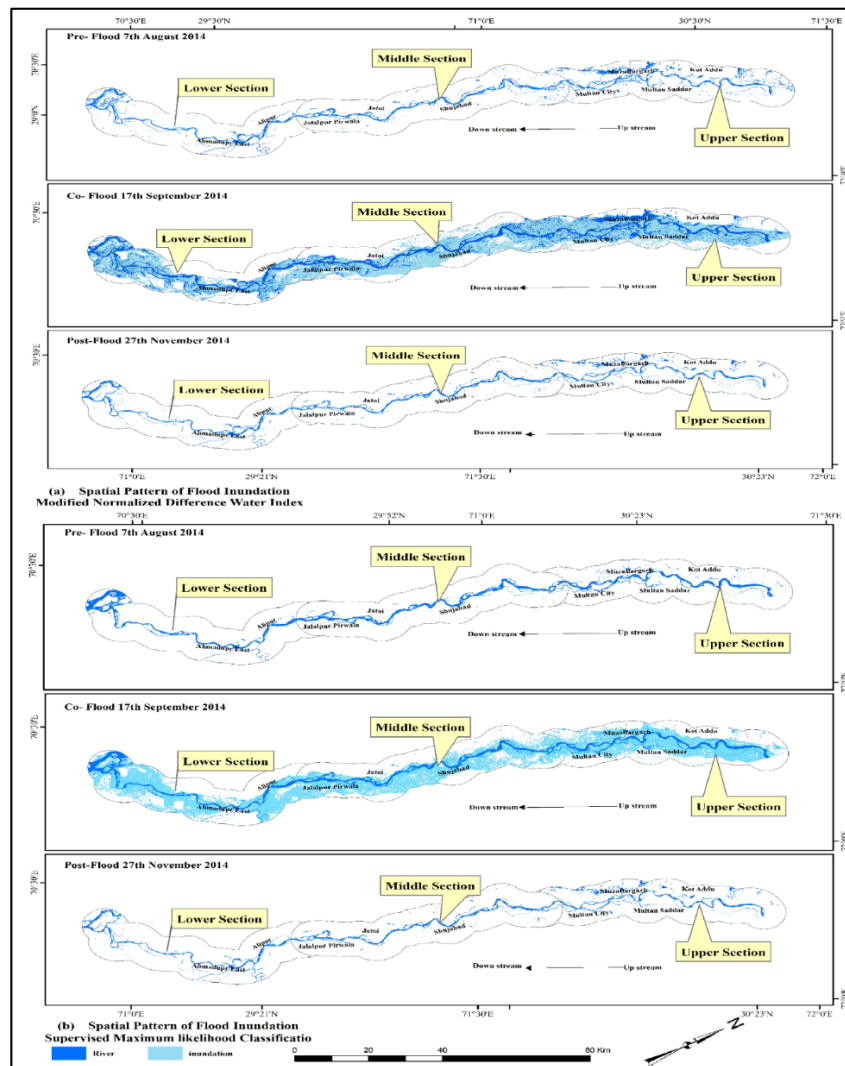
Figure 5.　Spatio-temporal flood inundation (**a**) using the MNDWI index (**b**) using Supervised Classification.

3.3. Land Use and Land Cover Changes

Figures 6–8 show the results of the supervised ML classification for land use/land cover mapping of Pre-flood (07 August), Co-flood (17 September), and Post-flood (27 November) images in the lower Chenab plain. We classified water, built-up, agriculture land and vegetation, barren land, sand, and deposited material on the pre- and post-flood images. However, deposited material was not identified in co-flood image due to intensive flood inundation (Figure 7). The results show significant changes in all classified land uses in relation to flood instances. In pre-flood, only 8% was covered by the water body, 17.39% of built up, 55.37% of vegetation/agriculture land, 4.84% of barren land,

8.32% of sand, and 5.92% of deposited material within a total area of 2536.11 km^2 (Figure 6). The water body showed only 8% in the pre-flood situation. However, after the flood occurrence in the month of September, 2014, an abrupt change appeared in the water body that represents a massive increase to 50% of the area, as shown in Figure 7. The massive water had not only inundated but also severely affected all other land uses. The built-up area considerably decreased from 17.39% to 11.85% in the study area. Likewise, we noticed a massive increase in water that affected the agriculture/vegetation covered area, which decreased from the initial total area of 2536.11 km^2, from 52.37% to 32.40%. The noticeable decrease of sand was from 8.3% to 1.1%. The slight decrease is noticed in barren land from 4.8% to 4%. Thus, the massive increase in water caused a large part of the agricultural/vegetation area to be flooded and destroyed most of the standing crops. In addition, the built-up area was also severely affected and flooded.
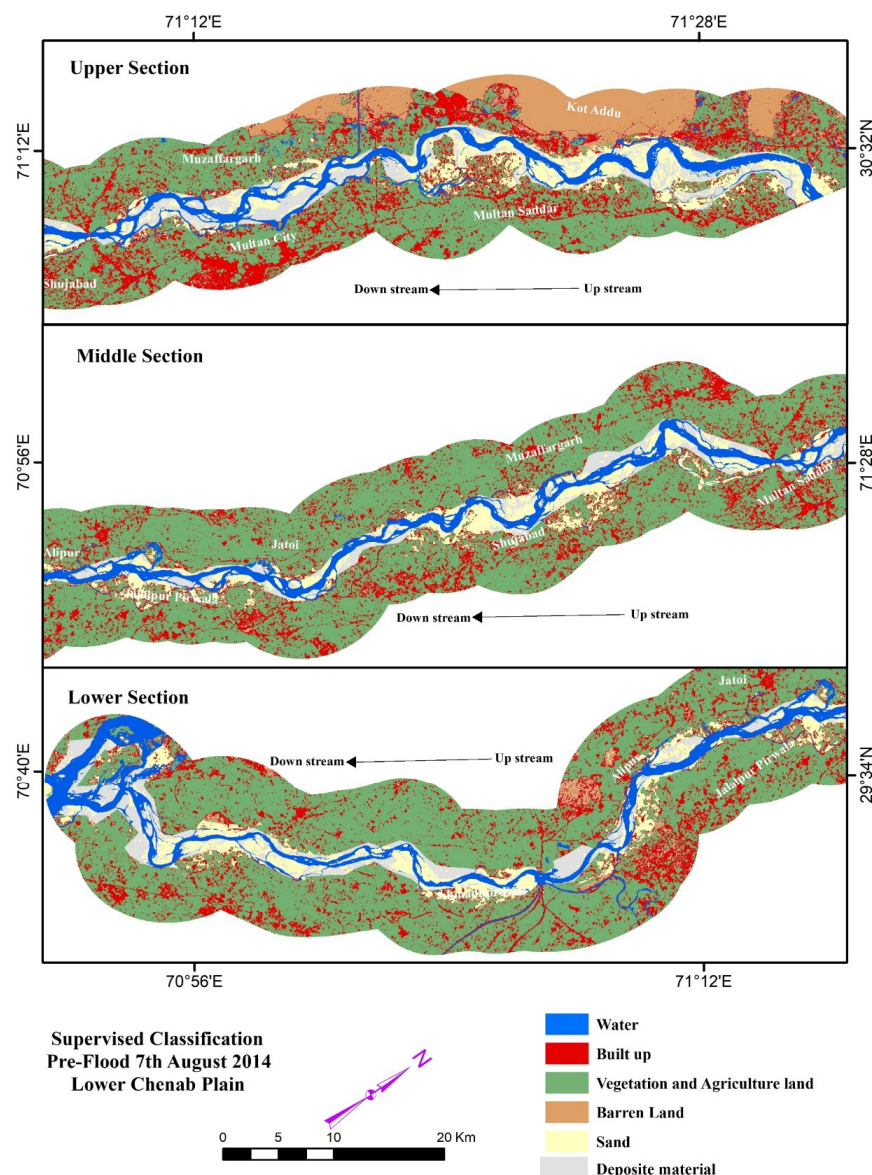
Figure 6. Land use/Land cover map of the pre-flood image developed using Landsat-8 images and supervised classification.
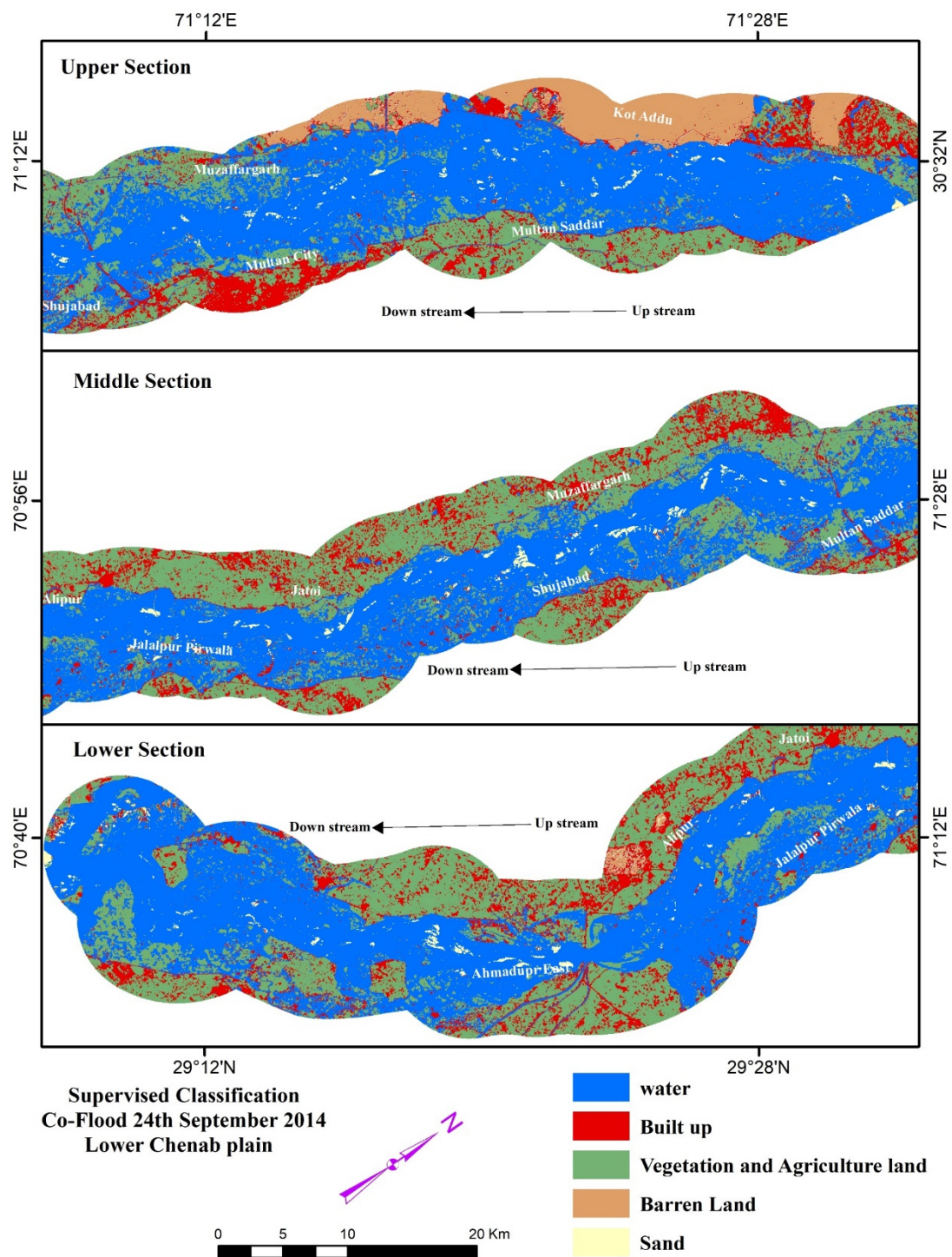
Figure 7. Land use/Land cover map of the co-flood image, 17 September, 2014, developed using Landsat-8 images and supervised classification.
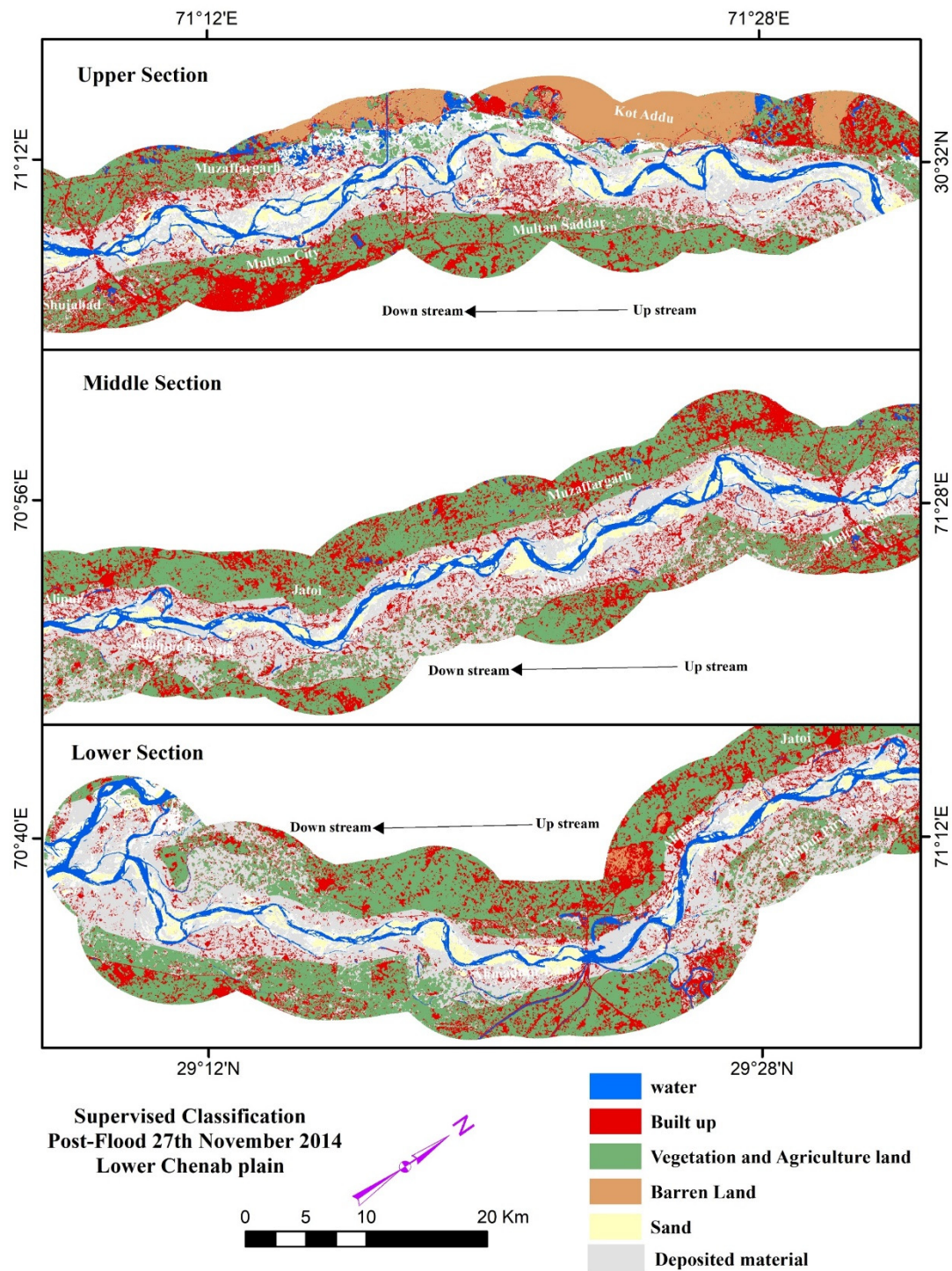
Figure 8. Land use/Land cover map of the post-flood image developed using Landsat-8 images and supervised classification.

In the post-flood period (Figure 8), water receded to its original pre-flood stage and decreased to only 6% from 50% in the co-flood image. Similarly, built up also regained its original pre-flood stage and increased to 17.79%. After the flood occurred, water receded back but large amounts of sediment and other materials remained, representing a dramatic increase from 5.92% to 30%. Similarly, an increase in the vegetation and agriculture area can be noticed from 32.40% to 37.50%. The barren land area did not change much as it remained constant in each instance. Sand slightly increased to 4.4% from 1.17% of total 2536.11 km^2 area, as shown in Figures 8 and 9. The total area in km^2 of each class is statistically

represented in Figure 9. Hence, all classified images show a similar pattern of land use/cover classes compared to high resolution GE images (Figure 10).
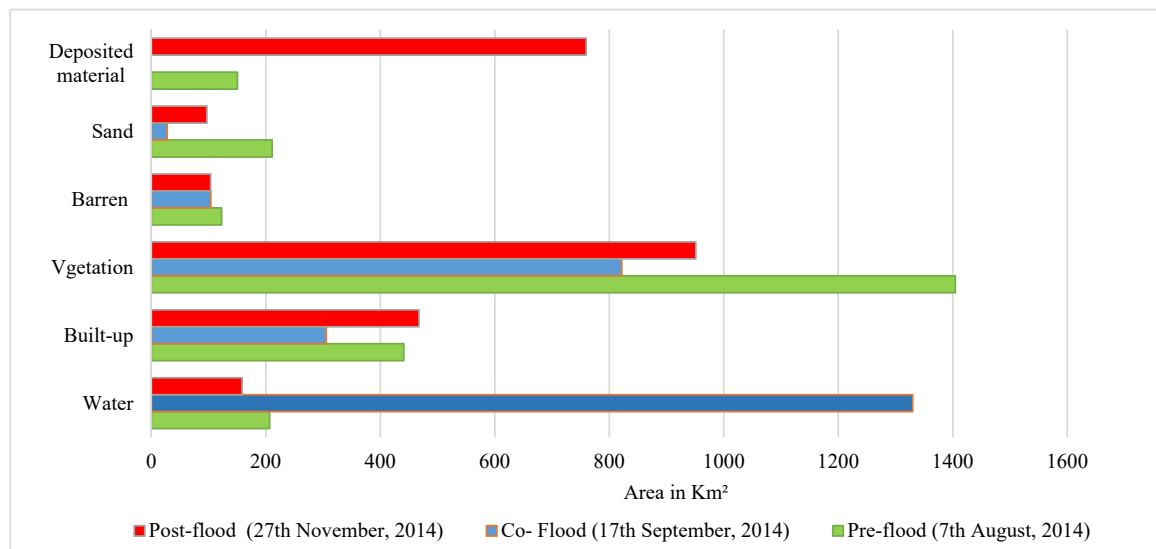

Figure 9. Change detection of land use/land cover in the lower Chenab plain using Landsat-8 flood instances images.

The classification result and GE images show the same pattern of land use changes in the study area. The agriculture and built-up areas along the river are clearly visible in the pre-flood image (Figure 10A). Conversely, the co-flood image (Figure 10B) depicts the abnormal change in water area that has increased drastically and caused an inundation to all the surrounding agricultural and built-up areas. As shown in Figure 10C the post-flood image shows the huge amount of deposited material along the river and its surrounding areas that dramatically increased and destroyed standing crops, which caused late sowing of agricultural crops, and further leads to low productivity in the study area.
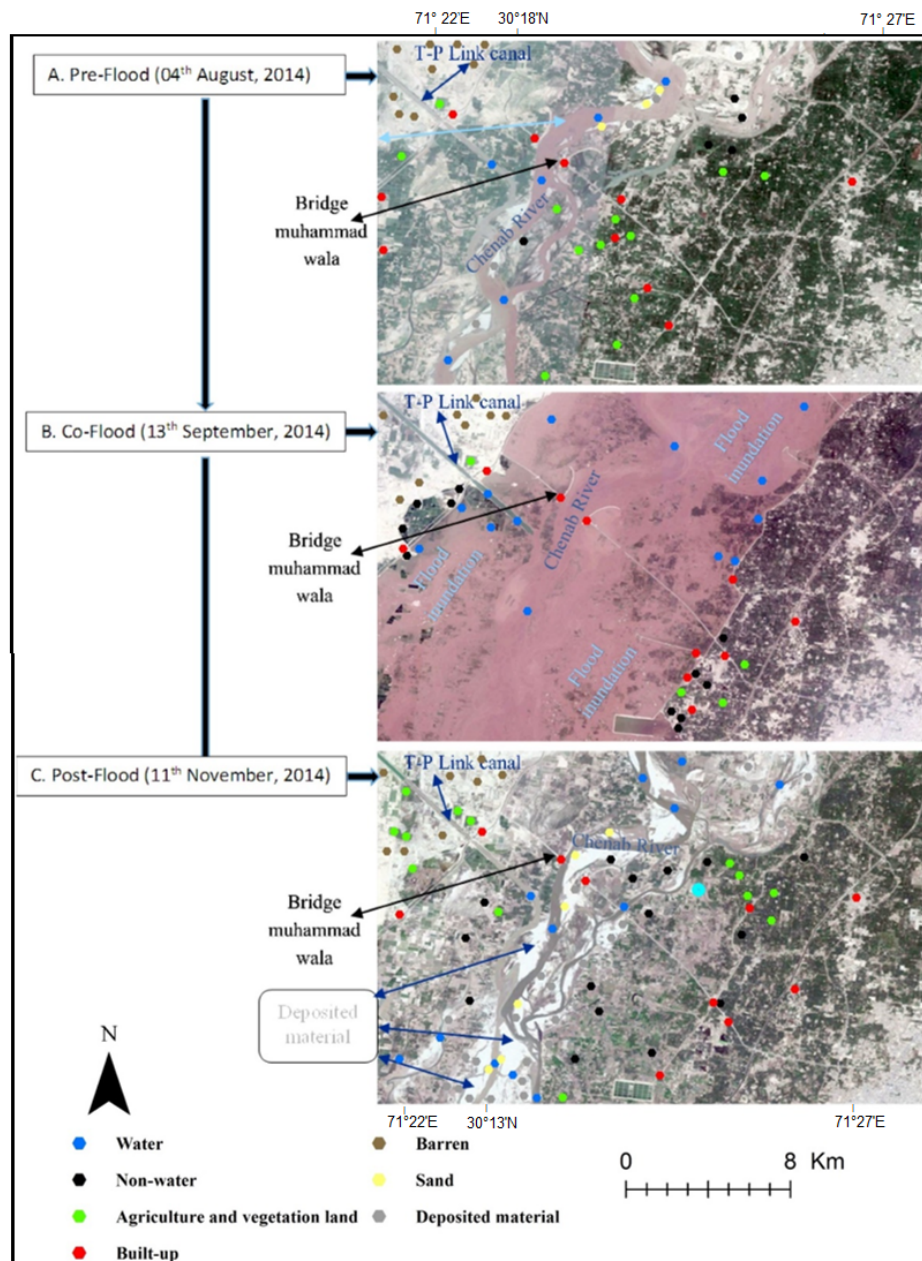
Figure 10. Google Earth 7.3.2.5776. (A. 4 August, 2014, B. 13 September, 2014, C. 11 November, 2014). Section 1, the lower Chenab plain. 30.290058° N,71.378478° E, Eye alt 11.42 mi. Also shown are validation points.

3.4. Damage Assessment

The results revealed that agriculture/vegetation areas were the most severely inundated, ~495 km^2, and while inundation in the built-up area covered 229 km^2, from the total inundated area of 1330 km^2, as shown in Figure 11a,b. The damage result further showed that a total of 361.43km^2 of agricultural land and 187.36km^2 of built-up areas were damaged due to deposited material. This result shows that the Multan district is the most affected/damaged district from flood-2014, as also shown in Figure 12a. Further details on the damaged agriculture land and built-up areas of the involved districts are listed in Figure 12b.
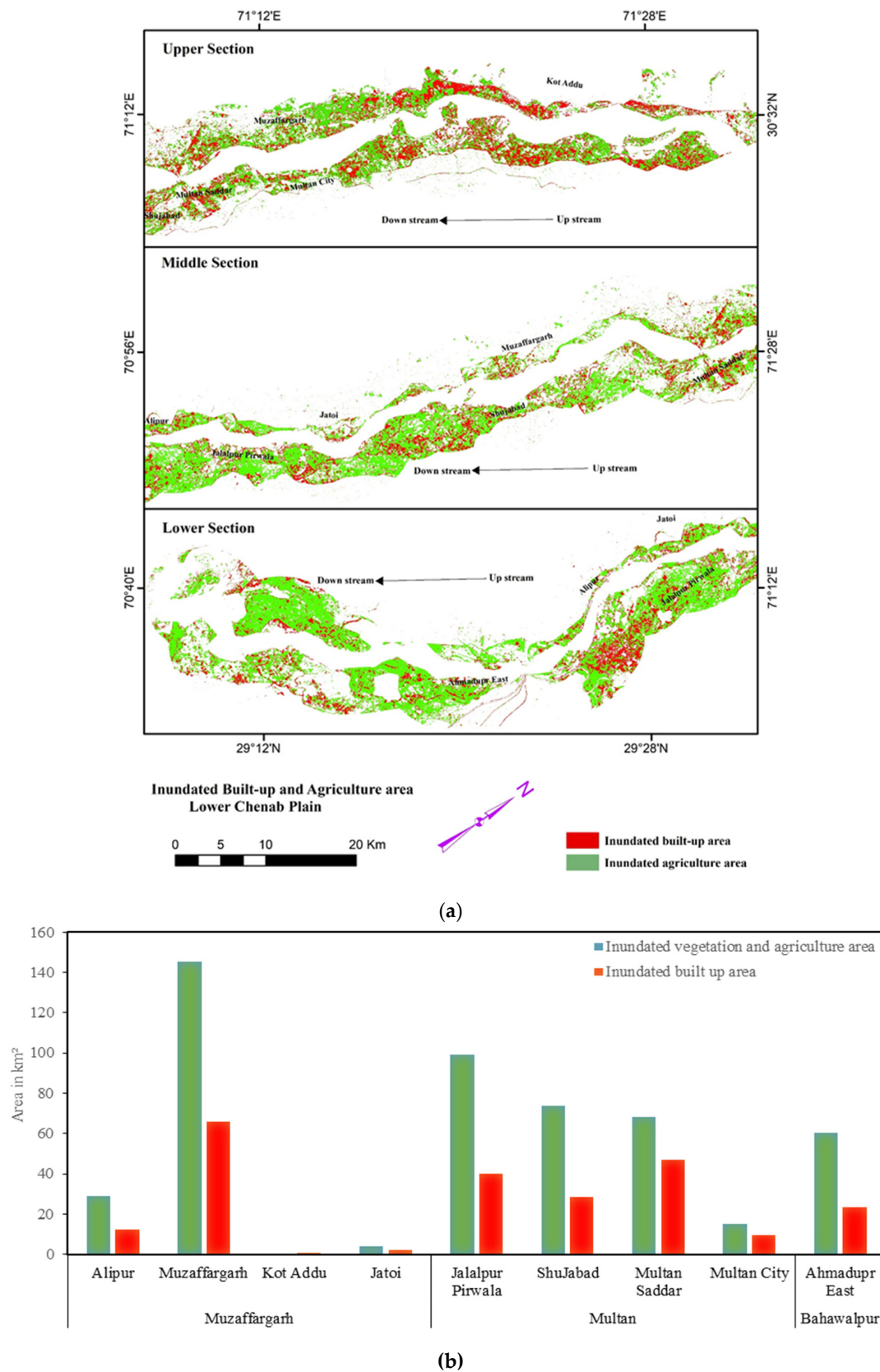
(**a**)

(**b**)

Figure 11. (**a**) Inundated agriculture and vegetation areas and built-up areas in the lower Chenab plain. (**b**) a graph of inundated agriculture and vegetation area, and built-up areas in the lower Chenab plain.
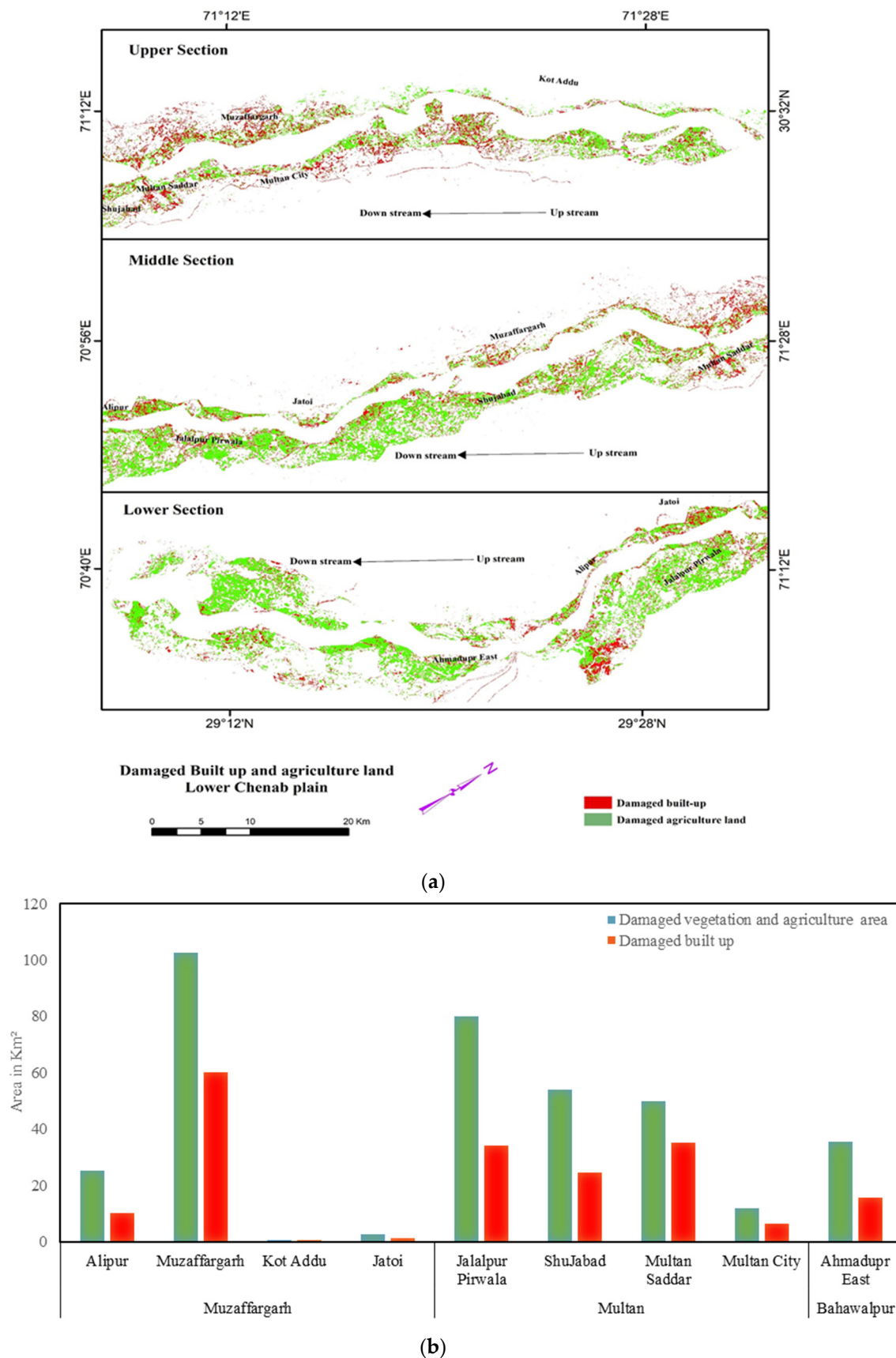
(**a**)

(**b**)

Figure 12. (**a**) Damaged agriculture and vegetation areas and built-up areas in the lower Chenab plain. (**b**) a graph of damaged agriculture and vegetation areas and built-up areas in the lower Chenab plain.

4. Discussion

Pakistan is a flood-prone country with historical records of various magnitudes of flood events [37,53,54]. In the past decade, flood disasters in Pakistan have surpassed all other disasters in terms of the frequency of occurrences, and also killed over 5700 people coupled with severe damages to the country's economy [5,12,15,17]. In the year of 2014, the flood started from late monsoon rainy season when the river Chenab inflow significantly increased from its upstream tributaries and resulted in high discharge, which exceeded the limits of the river flowing capacity and subsequently caused a huge inundation in the study area, as shown in Figures 7 and 10b.

Our results show that open satellite data coupled with an ML-supervised classification approach and the MNDWI allow the delineation of flood inundated and damaged areas with high overall accuracy. To obtain high accuracy levels, appropriate satellite data is critical. Firstly, temporal relationship between flood occurrence and satellite characteristics is an important parameter in flood modeling. For instance, a low-resolution (~250 m), multispectral Moderate Resolution Imaging Spectroradiometer (MODIS) satellite with its daily revisit time has already been used to obtain a co-flood image for certain flood events in Pakistan, but with questionable accuracy [19,55]. However, due to absence of any co-flood open access high resolution, e.g., Sentinel-1, for the study area, we opted to use moderate spatial resolution Landsat data (~30 m) for flood monitoring and assessment [9,18,22]. Despite a relatively better resolution, Landsat data are limited in such a way that they lack the timely acquisition of geospatial data, which sometimes reduces their suitability for flood monitoring and inundation mapping [26,39,56]. In the study area however, two adjacent Landsat satellite paths (150 and 151) made it possible to acquire high temporal resolution Landsat data (~7 days), against a single temporal resolution of 15 days for an area [9,18,57]. As such, the high temporal resolution of Landsat data enables a detailed investigation of operational flood mapping and monitoring in a study area. Secondly, existences of cloud cover can restrain the availability of flood instances images. Certainly, SAR (Sentinel 1,2,3) and RADAR satellites can easily penetrate clouds and acquire images in comparison to optical satellites (Landsat, MODIS) [26,58]. In our cases, the free SAR data were not available and the study area was entirely cloud free during the 2014 flood, since the causative meteorological events happened in upper Chenab plain. These events generated the flood peak that happened almost 10 days prior to the flooding in lower Chenab plain. Thirdly, consideration of land use/cover change of the flooded area is also an important factor in choosing the satellite data. The inundated agriculture and built-up area can easily be detected by most Radar SAT and optical satellites [59]. With multispectral Landsat images, we can recognize flooded areas even after several days of flood occurrence [41,42,56]. Nevertheless, we used Landsat-8 data as it is also possible to detect sediment material over agriculture fields and built-up areas with reliable accuracy [26,59]. Despite that, high resolution SAR data and a field survey are necessary for accurate and reliable flood mapping and damage assessment [59,60]. Finally, we have to consider the accuracy of the applied methods to the satellite data in order to ascertain the reliability of the flood monitoring results. This study produces an overall accuracy for the MNDWI index of almost 90% (Table 2), while classified images had an average overall accuracy of about 88% (Table 3). The water class attained the highest overall accuracy in this study, which has the ability to obtain a highest possible accuracy of 100% [49]. Despite that sand also shows reliable accuracy, in some occasions, wet sand was confused with water and vegetation/agriculture land. This is also noted in some instances where agriculture and built-up areas are also confused in transition areas due to mixed pixels.

During the flood-2014 event, the peak-flood water arrived on 17 September, 2014, and then remained constant for a while. The water slightly receded at a rate of 7 km^2/day, until 24 September, while a recharge of flood water continues from upstream areas. Here, the flood water started to decrease at a rate of 23km^2/day until 26 October, exposing a once flooded area of 636.35 km^2. On 27 November, the river regained its pre-flood stage and flowed normally. However, inundation remained for almost two months in the study area, as shown in Figure 4. As shown in Figures 11 and 12, the flood-2014 caused huge inundation and damages to agriculture land and built up in the study area.

The field survey reveals that most of the local people live in mud houses, which are highly vulnerable to flood disaster and have no flood resilience capacity [25]. As a result, already vulnerable mud houses were badly destroyed by the flood, besides infrastructure being destroyed by the gushing flood-2014. Moreover, the survey reveals that the month of November is considered agriculture land preparation and sowing season for new Rabi season crops and simultaneously harvesting season of certain kharif crops, such as sugarcane and rice in the study area. As a result, vegetation/agriculture land slightly increased to 37% in the post-flooding instance. Likewise, the built-up area also increased to 17.7%, which regained its pre-flood situation, probably due to the receded flood water and reconstruction. Furthermore, the survey shows that the Chenab river carried a huge amount of sediment material from its upstream mountainous areas, and it was ultimately deposited along the lower Chenab plain in 2014. However, deposited material immensely increased to 30% in the post-flooding instance (Figure 10). In our case, the field survey provided real-time reliable information, which is immensely required for comprehensive flood disaster assessment.

The moderate 30m resolution Landsat data that we used indicated that tracking inundated and damaged agriculture areas and built-up areas is reliable and acceptable. This mostly applies to damage assessment, which could be used for post-flood rehabilitation and a relief operation. However, for mapping the of detailed built up and agriculture area with a high overall accuracy, we must utilize high-resolution satellite data (RADARSAT, SAR), aerial photography, and extensive field survey, which are very often time and cost intensive and the required high-resolution satellite images are not open access. In this work, we did a field survey in order to evaluate real time damages, geo-location information, and the validation of Remote Sensing (RS) results. Thus, we correlated our survey findings for the validation of RS results and formulated an emergency damage assessment. Our damage analysis aims to provide a rapid and low-cost assessment of damaged agricultural and built-up areas but does not provide direct information on monetary losses and indirect damages, which may occur after flooding.

Landsat-8 data are affected by clouds, spectral sensitivity, and moderate spatial resolution and can only detect surface reflectance changes. Conversely, Radar satellite data can easily penetrate clouds and will perform properly in all weather conditions and detect changes in vegetation structure and moisture [59,60]. Radar data is more reliable when extracting flood inundation and damages in agricultural and built-up areas [25]. This well-known advantage allows Radar data to find the inundated and damaged areas in the post-flood stage in order to carry out an emergency flood damage assessment [58–60]. However, Radar data is costly and is not applicable for historical data analysis. However, despite such limitations, the integration of field and ancillary data allowed us to extract flood inundation and damage assessment with reliable accuracy. We noticed a number of factors that affected the tracking of damage assessment in this study. The lower Chenab floodplain contains numerous mangoes and other Bela forests. The co-flood Landsat image reveals that flood inundation beneath thin mangoes and other tree canopy covers was easily detected but thick or dense canopy covers' pixels were not identified due to the moderate resolution. This resulted in addition to the overall omission error and also caused the least identification of inundated areas in change detection analysis during flood instances. Secondly, a misclassification error was found in the classified images as the open land classified as the deposited material class in the post-flood image due to the moderate resolution and spectral sensitivity. Then, this error was removed and corrected through field-survey findings. Finally, the moderate 30-m spatial resolution of the Landsat images contributed to mix-up and misclassification in built-up areas where floodwaters pass through housing structures, roads, and other features. This increases the brightness of otherwise dark pixels (water), resulting in an increase in omission errors, which is a limitation for built-up damage assessments.

5. Conclusions

In this study, we presented a low cost and user-friendly flood monitoring and damage assessment with the integration of open access optical remote sensing and appropriate processing methods

jointly exploited with field data. In particular, we used Landsat-8 data and processed them with open-source, GIS-based, supervised classification for damage assessment and a satellite-derived MNDWI index for flood inundation and monitoring. The classified images and inundation mapping produced an excellent overall accuracy of about 90%, which is validated and shows reliable results. we conclude that these methods have been proven to be useful for estimating and understanding a future flood phenomenon with its diverse impacts. These methods do not require more time and provide near real-time information using the user input with indigenous knowledge and expertise. Furthermore, the classified result reveal that the agriculture sector has been the most affected land use/cover in the study area. In a large context, people are mostly engaged with agricultural activities, and this pattern of flood impacts are a major concern as it directly influences the livelihood of the floodplain community. The index result shows that about 75% of the area experienced severe flooding, which lies mostly in the southern and central part of study area, and further revealed that flood inundation remained for almost two months. Finally, despite the fact that flood disasters are recurrent phenomena, our study proves that the used datasets and methods can be useful for emergency, real-time, automated flood monitoring and damage assessment in order to formulate emergency flood disaster management, particularly for relief and response operations. In contrast, traditional flood monitoring and damage assessment with paid on-demand data provides comparatively accurate results, but it is a more resource- and time-consuming process.

Despite that our study is local to Pakistan, a few points from our results can be applied in other areas and thereby contribute to science and global perspectives on flooding. In this paper, we have shown that the existing supervised classification methods, combined with the MNDWI and ground-based validation point, can solve a problem of flooding and provide flood management solutions to local authorities. The combination of supervised classification and the MNDWI has contributed to the accurate mapping of flood extents using Landsat imagery. Despite that these two methods are mostly applied separately, the combined application in flood mapping can help to produce reliable results, with complimentary properties. Furthermore, in the unique agricultural environment along the river, the approach of combining two classification methods can provide insights into flood instances and inundation in both build up and agricultural areas, enabling a rapid check on damages to both built up and agricultural crops and thereby providing an estimation of loss that can support ground-based research. We have also shown that despite a low temporal resolution of Landsat images, the exploitation of two adjacent Landsat paths can provide a high temporal resolution, which can be applied not only to flood management and monitoring but also other fields that require high temporal resolution data, especially where another dataset is not available. This exploitation increased the temporal resolution by two-fold, from ~15 days to ~ 7 days, which can also be factored into operational flood monitoring for emergency responses, such as early response and relief operations. Thus, our study has given another perspective to flood monitoring and management using the available and free satellite imagery.

References

1.　Ward, P.J.; Jongman, B.; Weiland, F.S.; Bouwman, A.; van Beek, R.; Bierkens, M.F.; Ligtvoet, W.; Winsemius, H.C. Assessing flood risk at the global scale: Model setup, results, and sensitivity. *Environ. Res. Lett.* **2013**, *8*, 044019. [CrossRef]

2.　Schumann, G.; Bates, P.D.; Apel, H.; Aronica, G.T. Global Flood Hazard Mapping, Modeling, and Forecasting: Challenges and Perspectives. *Glob. Flood Hazard Appl. Model. Mapp. Forecast.* **2018**, 239–244.

3.　Iqbal, M.S.; Dahri, Z.H.; Querner, E.P. The impact of climate change on flood frequency and intensity in the Kabul River basin. *Geosciences* **2018**, *8*, 114. [CrossRef]

4.　Rahman, A.; Khan, A.N. Analysis of flood causes and associated socio-economic damages in the Hindu Kush region. *Nat. Hazards.* **2011**, *59*, 1239–1260. [CrossRef]

5.　Halgamuge, M.N.; Nirmalathas, A. Analysis of large flood events: Based on flood data during 1985–2016 in Australia and India. *Int. J. Disaster Risk Reduct.* **2017**, *24*, 1–11. [CrossRef]

6.　Milly, P.C.D.; Wetherald, R.T.; Dunne, K.A.; Delworth, T.L. Increasing risk of great floods in a changing climate. *Nature* **2002**, *415*, 514–517. [CrossRef] [PubMed]

7.　Islam, A.S.; Bala, S.K.; Haque, M. Flood inundation map of Bangladesh using MODIS time-series images. *J. Flood Risk Manag.* **2010**, *3*, 210–222. [CrossRef]

8.　Syvitski, J.P.; Brakenridge, G.R. Causation and avoidance of catastrophic flooding along the Indus River, Pakistan. *GSA Today* **2013**, *23*, 4–10. [CrossRef]

9.　Gaurav, K.; Sindha, R.; Panda, P.K. The Indus flood of 2010 in Pakistan: a perspective analysis using remote sensing data. *Nat. Hazards.* **2011**, *59*, 1815–1826. [CrossRef]

10.　Mahmood, S.; Rahman, A.; Sajjad, A. Assessment of 2010 flood disaster causes and damages in district Muzaffargarh, Central Indus Basin, Pakistan. *Environ. Earth Sci.* **2019**, *78*, 63. [CrossRef]

11.　Sajjad, A.; Lu, J.; Chen, X.; Chisenga, C.; Mahmood, S. The riverine flood catastrophe in August 2010 in South Punjab, Pakistan: Potential causes, extent and damage assessment. *Appl. Ecol. Environ. Res.* **2019**, *17*, 14121–14142.

12.　Federal Flood Commission Islamabad (FFCI). *Annual flood Report*; Ministry of Water and Power, Government of Pakistan: Islamabad, Pakistan, 2015.

13.　Atif, I.; Mahboob, M.; Waheed, A. Spatio-Temporal Mapping and Multi-Sector Damage Assessment of 2014 Flood in Pakistan using Remote Sensing and GIS. *Indian J. Sci. Technol.* **2015**, *8*, 35. [CrossRef]

14.　Ali, S.; Li, D.; Congbin, F. Twenty first century climatic and hydrological changes over upper Indus Basin of Himalayan region of Pakistan. *Environ. Res. Lett.* **2015**, *10*, 14007. [CrossRef]

15.　Rahman, A.; Khan, A.N. Analysis of 2010-flood causes, nature and magnitude in the Khyber Pakhtunkhwa, Pakistan. *Nat. Hazards.* **2013**, *66*, 887–904. [CrossRef]

16.　Mahmood, S.; Rani, R. Extent of 2014 flood damages in Chenab Basin Upper Indus Plain. In *Natural Hazards-Risk Assessment and Vulnerability Reduction*; Intech Open: London, UK, 2018. [CrossRef]

17.　Hashmi, H.N.; Siddiqui, Q.T.M.; Ghuman, A.R.; Kamal, M.A.; Mughal, H. a critical analysis of 2010 floods in Pakistan. *Afr. J. Agric. Res.* **2012**, *7*, 1054–1067.

18.　Khalid, B.; Cholaw, B.; Alvim, D.S.; Javeed, S.; Khan, J.A.; Javed, M.A.; Khan, A.H. Riverine flood assessment in Jhang district in connection with ENSO and summer monsoon rainfall over Upper Indus Basin for 2010. *Nat. Hazards* **2018**, *92*, 971–993. [CrossRef]

19.　Haq, M.; Akhtar, M.; Muhammad, S.; Paras, S.; Rahmatullah, J. Techniques of Remote Sensing and GIS for flood monitoring and damage assessment: a case study of Sindh province, Pakistan. *Egypt. J. Remote Sens. Space Sci.* **2012**, *15*, 135–141. [CrossRef]

20.　Pakistan Meteorological Department (PMD). *Annual Report*; Regional Meteorological Observatory: Lahore, Pakistan, 2015.

21.　Ashraf, M.; Shakir, A.S. Prediction of river bank erosion and protection works in a reach of Chenab River, Pakistan. *Arab. J. Geosci.* **2018**, *11*, 145. [CrossRef]

22.　Chohan, K.; Ahmad, S.R.; Islam, Z.; Adrees, M. Riverine flood damage assessment of cultivated lands along Chenab River using GIS and remotely sensed data: a case study of district Hafizabad, Punjab, Pakistan. *J. Geogr. Inf. Syst.* **2015**, *7*, 506–526. [CrossRef]

23.　National Disaster Management Authority((NDMA). *Annual Flood Report*; Regional office: Islamabad, Pakistan, 2015.

24.　Punjab Provincial Disaster Management Authority (PPDMA). *Annual Flood Report*; Regional Office: Lahore, Pakistan, 2015.

25. Moel, H.D.; Alphen, J.V.; Aerts, J. Flood maps in Europe–methods, availability and use. *Nat. Hazards Earth Syst. Sci.* **2009**, *9*, 289–301. [CrossRef]

26. Musa, Z.N.; Popescu, I.; Mynett, A. a review of applications of satellite SAR, optical, altimetry and DEM data for surface water modelling, mapping and parameter estimation. *Hydrol. Earth Syst. Sci.* **2015**, *19*, 3755–3769. [CrossRef]

27. Zhang, P.; Lu, J.; Feng, L.; Chen, X.; Zhang, L.; Xiao, X.; Liu, H. Hydrodynamic and Inundation Modeling of China's Largest Freshwater Lake Aided by Remote Sensing Data. *Remote Sens.* **2015**, *7*, 4858–4879. [CrossRef]

28. Bhatt, C.M.; Rao, G.S.; Farooq, M.; Manjusree, P.; Shukla, A.; Sharma, S.V.S.P.; Kulkarni, S.S.; Begum, A.; Bhanumurthy, V.; Diwakar, P.G.; et al. Satellite-based assessment of the catastrophic Jhelum floods of September 2014, Jammu & Kashmir, India. Geomatics. *Nat. Hazards Risk* **2016**, *8*, 309–327.

29. Chignell, S.M.; Anderson, R.S.; Evangelista, P.H.; Laituri, M.J.; Merritt, D.M. Multi-temporal independent component analysis and Landsat 8 for delineating maximum extent of the 2013 Colorado front range flood. *Remote Sens.* **2015**, *7*, 9822–9843. [CrossRef]

30. Lu, J.; Li, H.; Chen, X.; Liang, D. Numerical study of remote sensed dredging impacts on the suspended sediment transport in China's Largest Freshwater Lake. *Water* **2019**, *11*, 2449. [CrossRef]

31. Giustarini, L.; Chini, M.; Hostache, R.; Pappenberger, F.; Matgen, P. Flood Hazard Mapping Combining Hydrodynamic Modeling and Multi Annual Remote Sensing data. *Remote Sens.* **2015**, *7*, 14200–14226. [CrossRef]

32. Wulder, M.A.; Masek, J.G.; Cohen, W.B.; Loveland, T.R.; Woodcock, C.E. Opening the archive: How free data has enabled the science and monitoring promise of Landsat. *Remote Sens. Environ.* **2012**, *12*, 2–10. [CrossRef]

33. Sanyal, J.; Lu, X.X. Application of Remote Sensing in Flood Management with Special Reference to Monsoon Asia: a review. *Nat. Hazards* **2004**, *33*, 283–301. [CrossRef]

34. Hu, Q.; Wu, W.; Xia, T.; Yu, Q.; Yang, P.; Li, Z.; Song, Q. Exploring the use of Google Earth imagery and object-based methods in land use/cover mapping. *Remote Sens.* **2013**, *5*, 6026–6042. [CrossRef]

35. Twumasi, N.Y.D.; Shao, Z.; Altan, O. Mapping Built-Up Areas Using Two Band Ratio Onlandsat Imagery of Accra In Ghana From 1980 To 2017. *Appl. Ecol. Environ. Res.* **2019**, *17*, 13147–13168.

36. *Government of Punjab (GoP) Punjab Development Statistics*; Bureau of Statistics Government of Punjab: Lahore, Pakistan, 2015.

37. Siddiqui, M.; Haider, S.; Gabriel, H.F.; Shahzad, A. Rainfall–runoff, flood inundation and sensitivity analysis of the 2014 Pakistan flood in the Jhelum and Chenab river basin. *Hydrol. Sci. J.* **2018**, *63*, 13–14. [CrossRef]

38. Hansen, M.C.; Loveland, T.R. a review of large area monitoring of land cover change using Landsat data. *Remote Sens. Environ.* **2012**, *122*, 66–74. [CrossRef]

39. Munasinghe, D.; Cohen, S.; Huang, Y.F.; Tsang, Y.P.; Zhang, J.; Fang, Z.F. Intercomparison of Satellite Remote Sensing-Based Flood Inundation Mapping Techniques. *J. Am. Water Resour. Assoc.* **2018**, *54*, 834–846. [CrossRef]

40. Alphan, H.; Doygun, H.; Unlukaplan, Y.I. Post-classification comparison of land cover using multitemporal Landsat and ASTER imagery: The case of Kahramanmaras, Turkey. *Environ. Monit. Assess.* **2009**, *151*, 327–336. [CrossRef]

41. Rokni, K.; Ahmad, A.; Selamat, A.; Hazini, S. Water feature extraction and change detection using multitemporal Landsat imagery. *Remote Sens.* **2014**, *6*, 4173–4189. [CrossRef]

42. AlFaisal, A.; Kafy, A.A.; Roy, S. (Integration of Remote Sensing and GIS Techniques for Flood Monitoring and Damage Assessment: a Case Study of Naogaon District, Bangladesh. *J. Remote Sens. GIS* **2018**, *7*, 236.

43. Joyce, K.E.; Belliss, S.E.; Samsonov, S.V.; McNeill, S.J.; Glassey, P.J. a review of the status of satellite remote sensing and image processing techniques for mapping natural hazards and disasters. *Prog. Phys. Geogr.* **2009**, *33*, 183–207. [CrossRef]

44. Revilla-Romero, B.; Hirpa, F.A.; Pozo, J.T.; Salamon, P.; Brakenridge, R.; Pappenberger, F.; De Groeve, T. On the use of global flood forecasts and satellite-derived inundation maps for flood monitoring in data-sparse regions. *Remote Sens.* **2015**, *7*, 15702–15728. [CrossRef]

45. McFeeters, S.K. The use of the normalized difference water index (NDWI) in the delineation of open water features. *Int. J. Remote Sens.* **1996**, *17*, 1425–1432. [CrossRef]

46. Xu, H. Modification of normalized difference water index (NDWI) to enhance open water features in remotely sensed imagery. *Int. J. Remote Sens.* **2006**, *27*, 3025–3033. [CrossRef]

47. Fisher, A.; Flood, N.; Danaher, T. Comparing Landsat water index methods for automated water classification in eastern Australia. *Remote Sens. Environ.* **2016**, *175*, 167–182. [CrossRef]

48. Ho, L.T.K.; Umitsu, M.; Yamaguchi, Y. Flood hazard mapping by satellite images and SRTM DEM in the Vu Gia-Thu Bon alluvial plain, central Vietnam. *Arch. Photogramm Remote Sens.* **2010**, *38*, 275–279.

49. Elhag, M. Consideration of Landsat-8 spectral band combination in typical Mediterranean forest classification in Halkidiki, Greece. *Open Geosci.* **2017**, *9*, 468–479. [CrossRef]

50. Acharya, T.D.; Subedi, A.; Lee, D.H. Evaluation of Water Indices for Surface Water Extraction in a Landsat 8 Scene of Nepal. *Sensors.* **2018**, *18*, 2580. [CrossRef] [PubMed]

51. Zhou, S.L.; Zhang, W.C. Flood monitoring and damage assessment in Thailand using multi-temporal HJ-1A/1B and MODIS images. *IOP Conf. Ser. Earth Environ. Sci.* **2017**, *57*. [CrossRef]

52. Notti, D.; Giordan, D.; Caló, F.; Pepe, A.; Zucca, F.; Pedro Galve, J. Potential and Limitations of Open Satellite Data for Flood Mapping. *Remote Sens.* **2018**, *10*, 1673. [CrossRef]

53. Mahmood, S.; Khan, A.H.; Mayo, S.M. Exploring underlying causes and assessing damages of 2010 flash flood in the upper zone of Panjkora River. *Nat. Hazards* **2016**, *83*, 1213–1227. [CrossRef]

54. Mahmood, S.; Khan, A.H.; Ullah, S. Assessment of 2010 flash flood causes and associated damages in Dir Valley, Khyber Pakh-tunkhwa Pakistan. *Int. J. Disaster Risk Reduct.* **2016**, *16*, 215–223. [CrossRef]

55. Memon, A.A.; Muhammad, S.; Rahman, S.; Haq, M. Flood monitoring and damage assessment using water indices: a case study of Pakistan flood-2012. *Egypt. J. Remote Sens Space Sci.* **2015**, *18*, 99–106. [CrossRef]

56. Shuhua, Q.I.; Brown, D.G.; Tian, Q.; Jiang, L.; Zhao, T.; Bergen, K.M. Inundation Extent and Flood Frequency Mapping Using LANDSAT Imagery and Digital Elevation Models. *GIScience Remote Sens.* **2009**, *46*, 101–127.

57. Frazier, P.S.; Page, K.J. Water body detection and delineation with Landsat TM data. *Photogramm. Eng. Remote Sens.* **2000**, *66*, 1467.

58. Uddin, k.; Matin, M.A.; Meyer, F.J. Operational Flood Mapping Using Multi-Temporal Sentinel-1 SAR Images: a Case Study from Bangladesh. *Remote Sens.* **2019**, *11*, 1581. [CrossRef]

59. Pradhan, B.; Pirasteh, S.; Shafie, M. Maximum flood prone area mapping using RADARSAT images and GIS: Kelantan river basin. *Int. J. Geoinformatics* **2009**, *5*, 11–23.

60. Giordan, D.; Notti, D.; Villa, A.; Zucca, F.; Calò, F.; Pepe, A.; Dutto, F.; Pari, P.; Baldo, M.; Allasia, P. Low cost, multiscale and multi-sensor application for flooded area mapping. *Nat. Hazards Earth Syst. Sci.* **2018**, *18*, 1493–1516. [CrossRef]